Resolving ambiguities in core size determination of magnetic nanoparticles from magnetic frequency mixing data

Ali Mohammad Pourshahidi[1,2*], Ulrich M. Engelmann[3], Andreas Offenhäusser[1,2], and Hans-Joachim Krause[1,4,]

[1]Institute of Biological Information Processing, Bioelectronics (IBI-3), Forschungszentrum Jülich, Germany,
[2]Faculty of Mathematics, Computer Science and Natural Sciences, RWTH Aachen University,52062 Aachen, Germany,
[3]Department of Medical Engineering and Applied Mathematics, FH Aachen University of Applied Sciences, 52428 Jülich, Germany,
[4]Institute of Nano- and Biotechnologies (INB), FH Aachen University of Applied Sciences, 52428 Jülich, Germany
[*]Correspondence: a.pourshahidi@fz-juelich.de

Keywords: Magnetic nanoparticles; Frequency mixing magnetic detection; Langevin theory; Magnetic nanoparticle core size determination

Abstract

Frequency mixing magnetic detection (FMMD) has been widely utilized as a measurement technique in magnetic immunoassays. It can also be used for the characterization and distinction (also known as “colourization”) of different types of magnetic nanoparticles (MNPs) based on their core sizes. In a previous work, it was shown that the large particles contribute most of the FMMD signal. This leads to ambiguities in core size determination from fitting since the contribution of the small-sized particles is almost undetectable among the strong responses from the large ones. In this work, we report on how this ambiguity can be overcome by modelling the signal intensity using the Langevin model in thermodynamic equilibrium including a lognormal core size distribution $f_L(d_c,d_0,\sigma)$ fitted to experimentally measured FMMD data of immobilized MNPs. For each given median diameter d_0, an ambiguous amount of best-fitting pairs of parameters distribution width σ and number of particles N_p with $R^2 > 0.99$ are extracted. By determining the samples’ total iron mass, m_{Fe}, with inductively coupled plasma optical emission spectrometry (ICP-OES), we are then able to identify the one specific best-fitting pair (σ, N_p) one uniquely. With this additional externally measured parameter, we resolved the ambiguity in core size distribution and determined the parameters (d_0, σ, N_p) directly from FMMD measurements, allowing precise MNPs sample characterization.

1. Introduction

Magnetic nanoparticle particles (MNPs) have been used widely in different research areas with biomedical applications [1–5], for example as markers in biosensors [6,7], organ-confined cancer treatments through hyperthermia [8–10], tracers in magnetic particle imaging (MPI) [11,12] and contrast agents in magnetic resonance imaging (MRI) [13,14]. However, each application imposes different demands on the MNP properties [15]. In practice, the synthesized particles are characterized by various techniques. For example, the hydrodynamic diameter (d_h) is often determined using dynamic light scattering (DLS) [16,17], and the magnetization can be assessed using vibrating sample magnetometry (VSM) [17] or SQUID susceptometry [18]. Determination of the core size and analysis of the morphology of the MNPs is routinely performed with transmission electron microscopy (TEM) imaging technique [17,19]. With this method, one can measure the core diameter (d_c) of a few hundred to a thousand particles to obtain a discrete core size distribution [17]. As the edges of the particle core usually appear blurry in the TEM image, the choice of the threshold in automized image processing can remarkably influence the resulting core size distribution. In addition, TEM requires costly instrumentation and a complex and destructive sample preparation technique while yielding only local information on the 2D projection of the particles [17,20].

As stated above, TEM core size analysis only carries limited value for the size distribution of an entire sample since only a small portion of particles is routinely investigated. However, for most of the applications mentioned above, large ensembles of MNPs are employed, containing billions of particles ($\sim 10^{12}\,\frac{1}{mL}$). It has been shown that susceptibility measurement techniques constitute a promising tool for obtaining information on the core size distribution of the particles in a larger volume [20,21] than is usually used in TEM. Furthermore, the average (magnetic) core size can also be derived for the entire ensemble of MNPs from the magnetization curve using Chantrell fitting [22] or from x-ray diffraction (XRD) analysis using the Scherrer method [23].

The Frequency Mixing Magnetic Detection (FMMD) method has been widely used for different research activities in the area of magnetic biosensing [24–29]. Recently it was shown that it can also be used for the analysis of the core size distribution of a larger volume of magnetic nanoparticles [30]. Furthermore, in Ref. [30] it was discussed that the magnetic particles with larger core sizes ($d_C > 20$ nm) contribute most dominantly to the FMMD signal.

In this work, we further analyze the core size determination of ensembles of MNPs using FMMD measurements and fitting the results with a lognormally distributed core size-dependent Langevin model in thermodynamic equilibrium. We elaborate on the ambiguity which arises upon evaluation of the fitting results and propose a method for resolving this ambiguity using the amount of iron determined by inductively coupled plasma optical emission spectrometry (ICP-OES).

2. Theory

2.1. *Mathematical description of particle distribution*

The Langevin function has been widely used for modelling the ensemble of non-interacting magnetic nanoparticles. It is described as [31]

$$\mathcal{L}\,(\xi) = \coth(\xi) - \frac{1}{\xi} \tag{1}$$

where ξ is the dimensionless variable given as

$$\xi = \frac{m_p \mu_0 H}{k_B T} \tag{2}$$

with m_p being the particle magnetic moment, μ_0 denoting the permeability of vacuum, H the amplitude of the applied magnetic field, T the temperature and k_B the Boltzmann constant.

The contributing variable of the MNPs in the magnetic moment m_p strongly depends on the core diameter d_c of the particles and can be described using equation (3) considering spherical particles.

$$m_p = \frac{M_s \pi d_c^3}{6} \tag{3}$$

where M_s is the saturation magnetization.

It has been reported in the literature that the core size distribution of such particles can be well described by a lognormal distribution [22,32,33] which is given by

$$f_L(d_c, d_0, \sigma) = \frac{1}{\sqrt{2\pi} \cdot d_c \cdot \sigma} \cdot \exp(-\frac{ln^2(d_c/d_0)}{2\sigma^2}) \tag{4}$$

where d_0 indicates the median of the distribution and σ the standard deviation of the diameters. Thus the total magnetic moment of particle ensemble with lognormal distribution can be obtained through an integral over the distribution from equation (4) as follows:

$$m_{total} = N_p \int_0^\infty dd_c \cdot f_L\,(d_c, d_0, \sigma) \cdot m_p(d_c) \cdot \mathcal{L}\,(\frac{M_s \pi d_c^3}{6\,k_B T}\,\mu_0 H) \tag{5}$$

here, N_p denotes the number of particles.

2.2. *Frequency mixing magnetic detection*

The FMMD technique uses a dual-frequency excitation field employing a high and low frequency, respectively f_1 and f_2. When this dual-frequency excitation field is incident upon the ensemble of magnetic nanoparticles, their nonlinear magnetization curve results in the appearance of sum and difference mixing harmonics of the excitation field, $f_1 \pm n \cdot f_2$, where n is an integer number [34]. The average response at these mixing frequencies can be calculated for each mixing harmonic as reported in our previous work [30]. The calculation of the average response for even mixing components is performed using

$$m_{f1+n\cdot f2}(d_c) = \frac{M_s\pi d_c^3}{6} \cdot \frac{2}{k}\sum_{i=0}^{k} cos[2\pi(f_1 + n\cdot f_2)t_i] \cdot \mathcal{L}\left[\frac{M_s\pi d_c^3}{6k_BT}\,[B_0 + B_1 sin(2\pi f_1 t_i) + B_2 sin(2\pi f_2 t_i)]\right] \tag{6}$$

with *n* being an odd integer number (1, 3, 5 …). Similarly, the calculation of the average response for odd mixing components is done with equation

$$m_{f1+m\cdot f2}(d_c) = \frac{M_s\pi d_c^3}{6} \cdot \frac{2}{k}\sum_{i=0}^{k} sin[2\pi(f_1 + m\cdot f_2)t_i] \cdot \mathcal{L}\left[\frac{M_s\pi d_c^3}{6k_BT}\,[B_0 + B_1 \sin(2\pi f_1 t_i) + B_2 \sin(2\pi f_2 t_i)]\right] \tag{7}$$

with *m* being an even integer number (2, 4, 6…).

For small arguments, a Taylor expansion of the Langevin function can be performed, as shown in Ref. [34]. Small arguments are obtained not only for small excitation field amplitudes, but also for small core diameters d_c. In this limit of small particle sizes, the frequency mixing signal at frequency $f_1+2\cdot f_2$ is obtained from Taylor expansion as

$$m_{f1+2\cdot f2}(d_c) = \frac{M_s\pi d_c^3}{6}\left(\frac{M_s\pi d_c^3}{6k_BT}\right)^3 \cdot \frac{1}{60}\cdot B_1\cdot B_2^2 \quad \propto \quad d_c^{12} \tag{8}$$

for zero offset field B_0. It should be noted that for small particle core sizes d_c, the mixing signal at frequency $f_1+2\cdot f_2$ scales with the 12th power of the core diameter. Therefore, the contribution of small particles is completely negligible against the contribution of large ones.

3. Material and methods

3.1. Magnetic beads

Magnetic nanoparticle samples used during this study were procured from Micromod Partikeltechnologie GmbH (Rostock, Germany). We have used two different particle types with varying hydrodynamic diameters and both are dextran based particles having a plain OH surface coating: nanomag®-D SPIO has hydrodynamic size of $\mathrm{d_h} = 20$ nm and stock concentration of 25 mg/mL (Product code:79-00-201). synomag®-D has $\mathrm{d_h} = 70$ nm and concentration of 25 mg/mL (Product code: 104-19-701). The mentioned magnetic beads have been reported to show a Lognormal distribution according to [35,36]

3.2. ICP-OES measurements

For the determination of absolute iron content, we carried out ICP-OES measurements using iCAP 7600 device. The prepared sample materials were dissolved from each container through addition of a total amount of 2 mL HCl. The sample containers were rinsed several times with Milli-Q water, and each sample was combined in a 15 mL falcon tube. Each solution was made up of a total volume of 10 mL. Finally, three parallel dilutions of each digestion solution (10-fold diluted) were prepared and analyzed.

3.3. Frequency mixing magnetic detection setup

The FMMD measurements of the samples were performed using an in-house-built setup described in [27]. The experimental setup consists of a magnetic reader synthesizing the dual-frequency excitation signals and a detection chain including pre-amplification stage used for the case of digital demodulation. In this work, the digital demodulation measurement scheme was used which includes a National Instruments NI-USB 6251 data acquisition card and a PC. The sensing unit (i.e. measurement head) houses the high and low-frequency excitation coils and a differentially wound detection coil. Furthermore, as explained earlier, this particular module utilizes an electromagnet for the generation of a static offset magnetic field. The low-frequency excitation field (B_2) is 16 mT at a frequency (f_2) of 63 Hz and the high-frequency excitation field (B_1) is 1.2 mT at a frequency (f_1) of 40.5 kHz. The static offset magnetic field is generated through an electromagnet with a coil factor of 4.8 mT/A supplied from a current source Hewlett Packard HP 6032.

3.4. Calculation of the iron mass

In the case of Fe_3O_4 MNP dilution, the iron mass per sample can be calculated as follows, considering the binding ratio of iron, the density of Fe_3O_4 being 5175 kg/m^3, the weight percentage of iron in magnetite (determined from the molar mass of iron, M_{Fe} = 55.845 g/mol and of oxygen, M_O = 15.999 g/mol), and additional information on the size distribution f_L from equations (4 and 5):

$$m_{Fe} = \frac{3M_{Fe}}{3M_{Fe} + 4M_O} \cdot \rho_{Fe_3O_4} \cdot N_p \cdot \frac{\pi}{6} \cdot \int_0^\infty dd_c d_c^3 \, f_L\,(d_c, d_0, \sigma) \tag{9}$$

Assuming a lognormal distribution, the integral can be analytically solved, yielding:

$$\int_0^\infty dd_c d_c^3 \, f_L\,(d_c, d_0, \sigma) = d_0^3 \exp(\frac{9\sigma^2}{2}) \tag{10}$$

3.5. Sample preparation

The liquid suspension of magnetic bead samples was prepared by diluting a 10 µL volume of magnetic bead from a stock solution of 5 mg/mL concentration using 140 µL of Milli-Q water, leading to a final concentration of 0.33 µg/µL which includes the MNPs and their coating. Additionally, the same concentration was immobilized on to 5 mm 5 × 5 mm polyethylene (PE) filter procured from Senova Immunoassay Systems, Weimar, Germany. The immobilization process was achieved by initially coating a glass test tube using Sigmacote purchased from Sigma-Aldrich®, (this coating helps to reduce the unwanted binding of beads onto the glass surface in form of agglomerates) the dilution was prepared and a filter was placed inside the dilution. The excess fluid was evaporated in a desiccator at a temperature of 70 °C.

The samples of two different types of commercial magnetic beads of type synomag®-D with d_h of 70 nm (named *Syn70*) and nanomag®-D SPIO with d_h of 20 nm (named *ND20*) were prepared with final MNP concentration of 0.33 µg/µL .

3.6. *Measurement procedure and data processing*

The FMMD signals of the prepared samples were measured using the setup described in section 3.3 according to the protocol described in [27].

Post-processing of the measured data including subtraction of the measured background signal and frequency-dependent phase correction in the complex plane was done using an in-house developed Python script. Unit conversion of the signal intensity from the measured signal amplitude in mV to the sample's nonlinear magnetic moment in nAm^2 was performed using the calibration factor obtained by the method presented in Refs. [27,30].

4. Results and discussion

4.1. *Measurement and Fit*

The static offset magnetic field was varied from 0 to 24 mT in steps of 1 mT. Figure 1 shows the offset-dependent nonlinear magnetization response of the samples *Syn70* and *ND20* for the first four mixing terms $f_1 + nf_2;\ n = \{1,2,3,4\}$. The measurement results for these samples are depicted as solid red circles and solid black squares, respectively. To determine the average core size parameters, with the assumption of a lognormal distribution of the core sizes, each measurement was fitted using the model of calculating the nonlinear magnetic moments according to Eqs. (6) and (7), integrated over a lognormal distribution (4) with three fitting parameters, $m(d_0,\sigma,N_p)$, through a nonlinear least square Levenberg-Marquardt optimization algorithm. The respective fits to each measurement are also depicted as a solid line with matching colors in Figure 1. The fitted theoretical signals agree very well with the measurement data, with $R^2 > 0.99$.

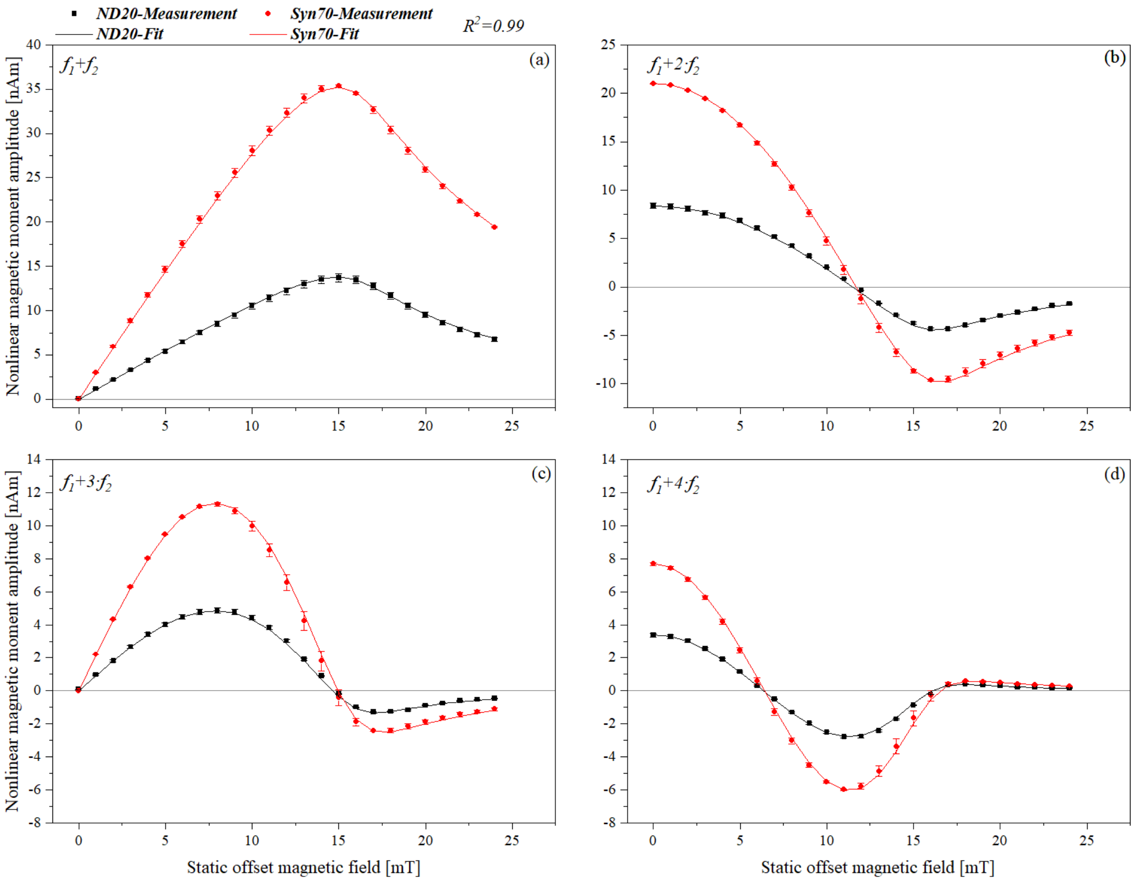

Figure 1. Measured first four nonlinear magnetic moment responses of samples Syn70 and ND20 with MNP concentration of 0.33 µg/µL at mixing frequencies a) $f_1 + f_2$, b) $f_1 + 2{\cdot}f_2$, c) $f_1 + 3{\cdot}f_2$ and d) $f_1 + 4{\cdot}f_2$ over a static magnetic offset field range from 0 to 24 mT. The red-filled circles represent the measurement data of the sample Syn70 and the solid red line represents the fitting to the respective measurement data. The black squares represent the measurement data of ND20 and the black solid line represents the fitting.

The parameters obtained from fitting to the Syn70 sample were $d_0 = 6.26$ nm, $\sigma = 0.37$ and $N_p = 4.0\times10^{13}$, the result of the ND20 fit was $d_0 = 5.86$ nm, $\sigma = 0.4$ and $N_p = 1.4\times10^{13}$.

However, it was found that the convergence of fits depended strongly on the choice of starting values. For further analysis, we therefore examined a wide range of median diameters d_0 between 5 nm and 18 nm, and a range of width parameters σ from 0.1 to 0.4. For fixed pairs (d_0, σ) in these ranges, we fitted just the amplitude N_p and plotted the fit quality R^2 in a contour plot as a function of d_0 and σ, see Figure 2 (a). It is clearly seen that a "ridge" of pairs (d_0, σ) yield excellent fits to the experimental data depicted in Figure 1 (a), with $R^2 > 0.99$. The "ridge top", i.e. the σ values which give maximum R^2 for a given d_0, is marked by the solid cyan line. The lognormal core size distributions corresponding to the coloured squares on that line are shown in Figure 2 (b).

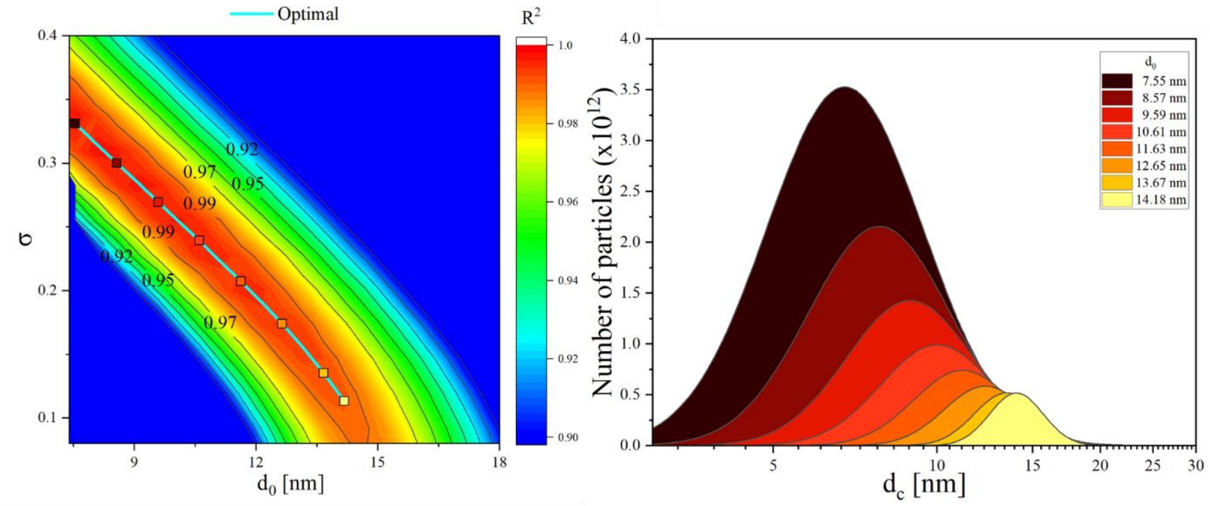

Figure 2. a) The contour plot of the R^2 values for different combinations of the parameters d_0 and σ, the optimal parameter line (with $R^2 > 0.99$) is depicted as a solid cyan line for the sample Syn70, b) The lognormal distribution of the optimal parameters which results in $R^2 > 0.99$, the legend shows different medians of the core size distributions. The corresponding (d_0,σ) combinations have been marked with respective colours on the optimal parameter line in (a).

The different lognormal core size distributions depicted in Figure 2 (b) all yield simulated FMMD signals which resemble very well the measured data (with $R^2 > 0.99$). So there is an ambiguity in core size determination of the sample from FMMD measurement, the inverse problem is ill-posed. The reason for this is that small particles have an almost negligible contribution to the signal since their signal scales with the 12th power of particle core diameter, $\propto d_c^{12}$, see Eq. (8). A wide distribution with a small median diameter (for instance the dark brown distribution for $d_0 = 7.55$ nm in Figure 2 (b)) has an enormous number of small particles which practically don't contribute to the FMMD signal, but do yield a considerable contribution to the iron mass (which scales with the 3rd power of diameter,$\propto d_c^3$). The FMMD signal is constituted only from the relatively small amount of larger particles in that distribution. In contrast, all particles of a narrow distribution with a large median diameter (for instance the bright yellow distribution for $d_0 = 14.18$ nm in Figure 2 (b)) contribute strongly to the FMMD signal. Therefore, the light yellow distribution needs much less iron to produce the same FMMD signal compared to the dark brown distribution with its multitude of non-contributing small particles, as for $d_0 = 14.18$ nm, the iron is favorably arranged in larger particles. We propose to resolve this fitting ambiguity by an independent determination of the total iron content of the sample. From all the possible distributions depicted in Figure 2 (b), we choose the one matching the measured amount of iron.

One can calculate the mass of iron (m_{Fe}) for all the distributions on the optimal parameter line using Eqs. (9) and (10). This was done by constraining the median core size d_0 and finding the best-fitting σ and N_p, leading to $R^2 > 0.99$. The true absolute amount of iron of the measured sample was determined by ICP-OES. Combining the FMMD measurement analysis for different distributions and the calculated iron mass, we generate a look-up graph, which relates a combination of (d_0, σ) marked with black squares uniquely to a number of particles (plotted as red squares) and thus to an iron mass (blue squares), respectively. This allows to one uniquely select the particle size distribution for which the measured iron mass (in our case obtained from ICP-OES) equals the calculated one. Figure 3 shows the look-up graph for the *Syn70* sample, in which the measured amount of iron was $(17.73 \pm 0.19)\ \mu g$. The point of intersection was determined through a linear interpolation between the two neighbouring points. The analysis reveals the size distribution with parameters $d_0 = 10.6$ *nm*, $\sigma = 0.24$ and $N_p = 5.8 \cdot 10^{12}$.

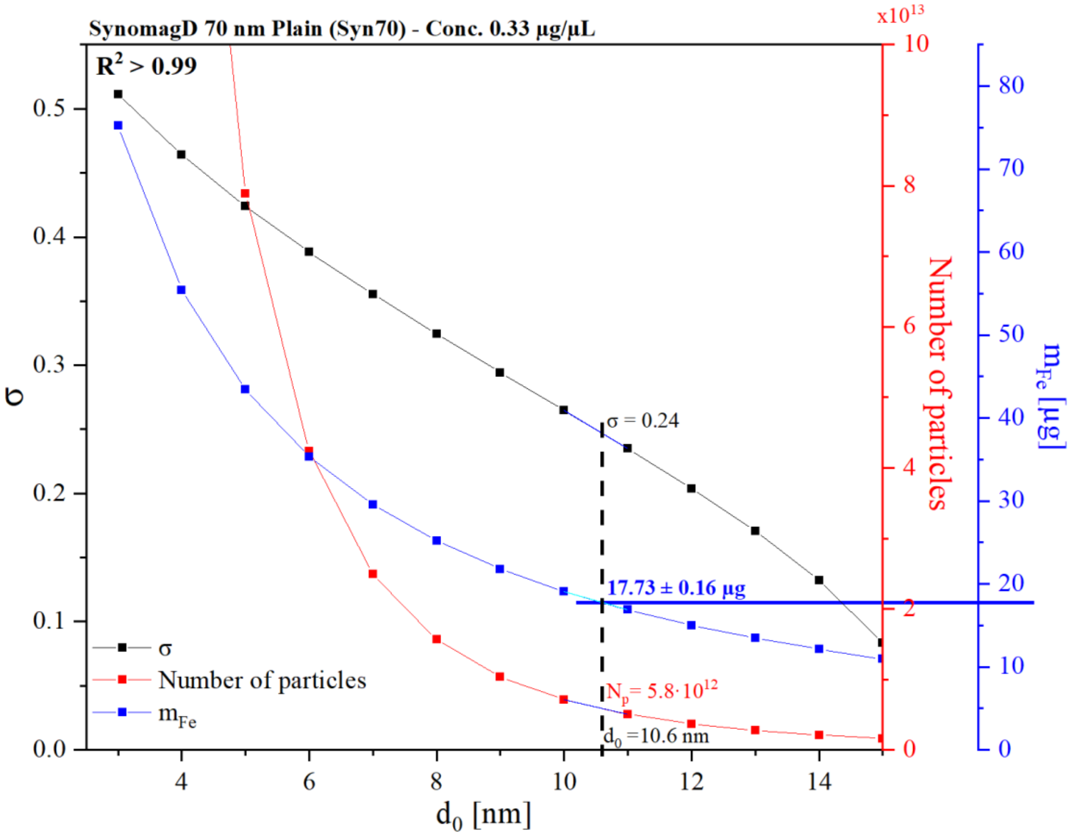

Figure 3. Look-up graph of sample Syn70, for the best combinations of the magnetic core size distribution (d_0, σ, N_P) leading to $R^2 > 0.99$. The σ values are depicted as black squares. The number of particles N_p are depicted as red squares and the calculated m_{Fe} are depicted as blue squares. The measured iron mass through ICP-OES is marked using a blue line. The intersection points are marked using a dashed line. For each parameter, the points are connected to guide the eye.

The same process was repeated to analyze the measurement of the sample *ND20* presented in Figure 4. The result of the analysis yields a d_0 = 13.5 nm with σ = 0.16 and $N_p = 8.4 \cdot 10^{11}$. The results for both samples are listed in Table 1.

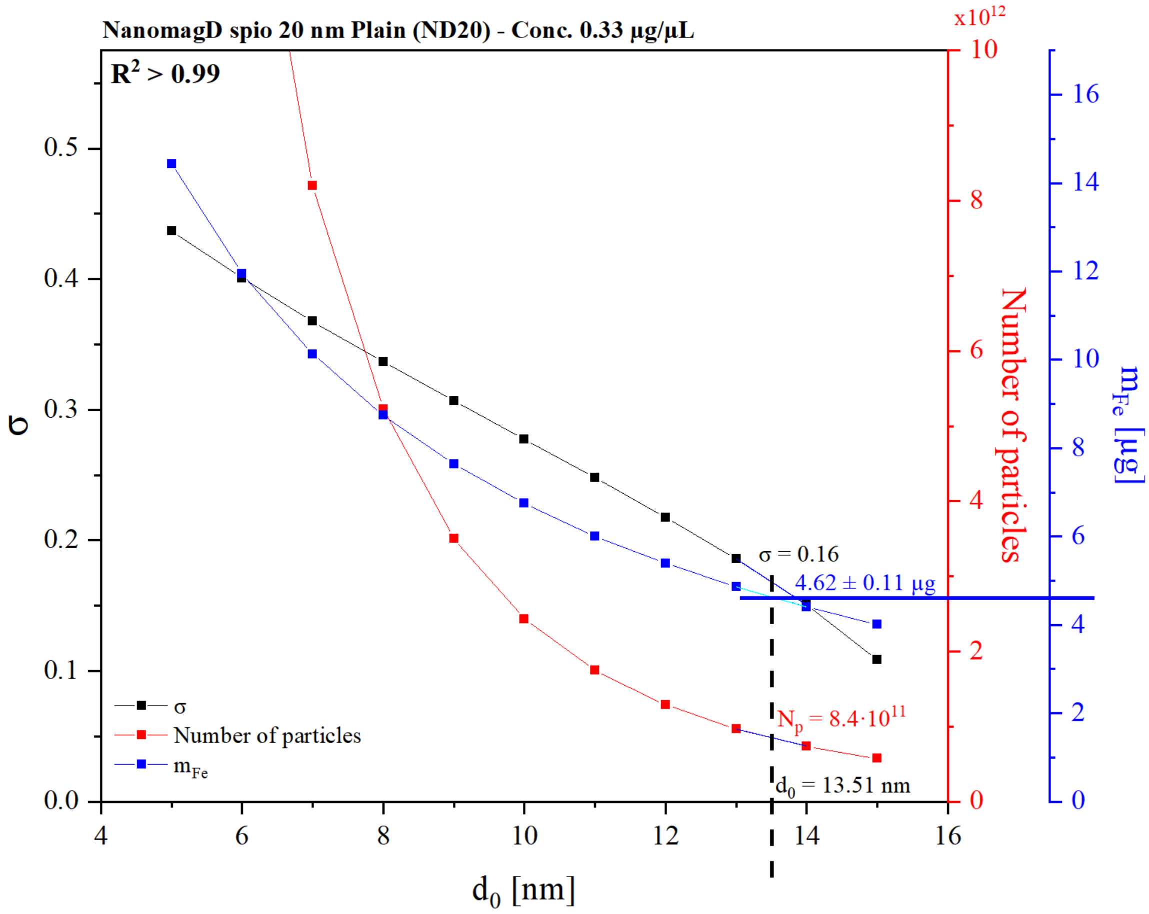

Figure 4. Look-up graph of ND20, for the best combinations of the magnetic core size distribution (d_0, σ, N_P) leading to $R^2 > 0.99$. The σ values are depicted as black squares. The number of particles N_P are depicted as red squares and the calculated m_{Fe} are depicted as blue squares. The measured amount of iron through ICP-OES is marked using a blue line. For each parameter, the points are connected for better visual aid.

Table 1. Iron mass of the samples measured with ICP-OES, and lognormal distribution parameters of the particles' core sizes obtained from this iron content.

Sample	***d_h [nm]***	***Measured m_{Fe} [µg]***	***Determined d_0 [nm]***	***Determined σ***	***Determined N_p***
Syn70	70	17.73 ± 0.19	10.6	0.24	$5.8 \cdot 10^{12}$
ND20	20	4.62 ± 0.11	13.5	0.16	$8.4 \cdot 10^{11}$

For comparison, the core sizes reported in the literature for the MNPs used here are slightly smaller. For synomag-D 70 nm particles, Ref. [37,38] reported an individual core size of 8.2 nm from analysis of TEM micrographs. In the case of nanomag-D SPIO 20 nm, Ref. [39] gave a core size of 11.2 nm obtained from an analysis of the DC magnetization curve from a Magnetic Property Measurement System (MPMS). Ref [40] reported a diameter range of 10-20 nm and [36] gave a number-average diameter of 8.1 ± 4 nm and a "weight-average diameter of 13 nm" based on TEM analysis. Additionally, [41] reported an XRD diameter of 8 ± 1 nm. For both particle types, our FMMD analysis yielded comparable values to the reported results in the literature, on average a few nanometer larger core sizes, but within the range of the reported diameters. A possible reason for the deviations may be the fact that our FMMD analysis forces the core size distribution to be lognormal. If the particle distribution is different, for instance bimodal, the mathematical determination of iron mass would be erroneous. In addition, our theoretical description is based on the assumption that all the atoms in a particle contribute to the particle's magnetic moment, without any non-interacting amorphous boundary layer. Additionally, our approach assumes non-interacting particles, whereas in reality, the particle interactions may result in altered magnetic characteristics and a more complex situation (e.g. changing magnetization [42], magnetic relaxation behavior [43] and especially magnetic anisotropy[44]). In addition, the precision of all the different measurement techniques TEM, MPMS, XRD and FMMD is limited. The error of each technique is at least 1 to 2 nm, so it can be concluded that the results do agree within the error limits.

5. Conclusions

Offset-field-dependent FMMD measurements were performed for two different MNP types. Core size distribution analysis was performed by fitting the calculated signals from the Langevin theory with lognormally distributed core sizes to the measurements. Further analysis revealed an ambiguity in the evaluation of the fitting results, leading to a number of equally well-suited fitting results for different combinations of median size d_0, size distribution width σ and number of particles per sample N_p, all of which yielded excellent agreement with measured data. The ambiguity was successfully resolved by measuring the total iron mass of the samples using ICP-OES and translating the iron mass in a look-up graph using the parameters of the fitting function and the calculated m_{Fe}. This graph allows to one uniquely select the one combination of (d_0, σ, N_p) with the measured amount of iron directly and reproducibly.

In future, this method should be further verified using alternative iron amount determination techniques such as photometry using a suitable iron-indicator (e.g. phenanthroline). Furthermore, improved accuracy could be achieved by including additional external parameters such as the saturation magnetization M_s of the sample which could be determined by VSM.

Overall, once this method is established, i.e. having reliable look-up-graphs for commonly used samples, a single determination of iron mass can then complete the full characterization of a unique sample (MNP ensemble) by directly yielding the underlying core-size distribution from an FMMD measurement. This would render FMMD as a highly effective MNP characterization method, as many biomedical applications of MNPs (s. section 1) are dominated by core-size effects, e.g. MPI [45,46] and MNP-mediated hyperthermia [47,48] .

Acknowledgements

The authors thank Dr. Stephan Küppers and Volker Nischwitz (ZEA-3) for the ICP-OES measurements, Norbert Wolters (IBI-TAV) for designing and assembling the readout electronics, and Dieter Lomparski (IBI-3, all Forschungszentrum Jülich) for the construction of the mechanical components and for his assistance in creating the data acquisition software.

Funding

This research was funded by the state of North Rhine-Westphalia and the European Regional Development Fund (ERDF; German: EFRE) under grant number EFRE-0801299, reference number LS-2-1-014c. The APC was funded by Forschungszentrum Jülich GmbH. U.E. was funded by German Federal Ministry of Culture and Science of North Rhine-Westphalia, grant Karrierewege FH-Professur.

Conflicts of Interest

The authors declare no conflict of interest. The funders had no role in the design of the study; in the collection, analyses, or interpretation of data; in the writing of the manuscript, or in the decision to publish the results.

Data Availability Statement

The data presented in this study are available on request from the corresponding author.

References

1. Chen, Y.-T.; Kolhatkar, A.G.; Zenasni, O.; Xu, S.; Lee, T.R. Biosensing Using Magnetic Particle Detection Techniques. *Sensors* **2017**, *17*, 2300, doi:10.3390/s17102300.
2. Rezvani Jalal, N.; Mehrbod, P.; Shojaei, S.; Labouta, H.I.; Mokarram, P.; Afkhami, A.; Madrakian, T.; Los, M.J.; Schaafsma, D.; Giersig, M.; et al. Magnetic Nanomaterials in Microfluidic Sensors for Virus Detection: A Review. *ACS Appl. Nano Mater.* **2021**, *4*, 4307–4328, doi:10.1021/acsanm.1c01077.
3. Krishnan, K.M. Biomedical Nanomagnetics: A Spin Through Possibilities in Imaging, Diagnostics, and Therapy. *IEEE Trans Magn* **2010**, *46*, 2523–2558, doi:10.1109/TMAG.2010.2046907.
4. Dadfar, S.M.; Roemhild, K.; Drude, N.I.; von Stillfried, S.; Knüchel, R.; Kiessling, F.; Lammers, T. Iron Oxide Nanoparticles: Diagnostic, Therapeutic and Theranostic Applications. *Adv Drug Deliv Rev* **2019**, *138*, 302–325, doi:10.1016/j.addr.2019.01.005.
5. Pankhurst, Q.A.; Thanh, N.T.K.; Jones, S.K.; Dobson, J. Progress in Applications of Magnetic Nanoparticles in Biomedicine. *J. Phys. D: Appl. Phys.* **2009**, *42*, 224001, doi:10.1088/0022-3727/42/22/224001.
6. Ha, Y.; Ko, S.; Kim, I.; Huang, Y.; Mohanty, K.; Huh, C.; Maynard, J.A. Recent Advances Incorporating Superparamagnetic Nanoparticles into Immunoassays. *ACS Appl Nano Mater* **2018**, *1*, 512–521, doi:10.1021/acsanm.7b00025.
7. Huang, S.-H.; Juang, R.-S. Biochemical and Biomedical Applications of Multifunctional Magnetic Nanoparticles: A Review. *J Nanopart Res* **2011**, *13*, 4411–4430, doi:10.1007/s11051-011-0551-4.
8. Engelmann, U.M.; Roeth, A.A.; Eberbeck, D.; Buhl, E.M.; Neumann, U.P.; Schmitz-Rode, T.; Slabu, I. Combining Bulk Temperature and Nanoheating Enables Advanced Magnetic Fluid Hyperthermia Efficacy on Pancreatic Tumor Cells. *Sci Rep* **2018**, *8*, 13210, doi:10.1038/s41598-018-31553-9.
9. Engelmann, U.M.; Fitter, J.L.; Baumann, M. Assessing Magnetic Fluid Hyperthermia : Magnetic Relaxation Simulation, Modeling of Nanoparticle Uptake inside Pancreatic Tumor Cells and in Vitro Efficacy, Infinite Science Publishing, 2019.
10. Kozissnik, B.; Bohorquez, A.C.; Dobson, J.; Rinaldi, C. Magnetic Fluid Hyperthermia: Advances, Challenges, and Opportunity. *International Journal of Hyperthermia* **2013**, *29*, 706–714, doi:10.3109/02656736.2013.837200.
11. Sehl, O.C.; Gevaert, J.J.; Melo, K.P.; Knier, N.N.; Foster, P.J. A Perspective on Cell Tracking with Magnetic Particle Imaging. *Tomography* **2020**, *6*, 315–324, doi:10.18383/j.tom.2020.00043.
12. Herynek, V.; Babič, M.; Kaman, O.; Charvátová, H.; Veselá, M.; Šefc, L. Development of Novel Nanoparticles for MPI. *International Journal on Magnetic Particle Imaging* **2020**, *6*, doi:10.18416/IJMPI.2020.2009019.
13. Caspani, S.; Magalhães, R.; Araújo, J.P.; Sousa, C.T. Magnetic Nanomaterials as Contrast Agents for MRI. *Materials (Basel)* **2020**, *13*, 2586, doi:10.3390/ma13112586.
14. Avasthi, A.; Caro, C.; Pozo-Torres, E.; Leal, M.P.; García-Martín, M.L. Magnetic Nanoparticles as MRI Contrast Agents. *Top Curr Chem (Cham)* **2020**, *378*, 40, doi:10.1007/s41061-020-00302-w.

15. Dadfar, S.M.; Camozzi, D.; Darguzyte, M.; Roemhild, K.; Varvarà, P.; Metselaar, J.; Banala, S.; Straub, M.; Güvener, N.; Engelmann, U.; et al. Size-Isolation of Superparamagnetic Iron Oxide Nanoparticles Improves MRI, MPI and Hyperthermia Performance. *J Nanobiotechnol* **2020**, *18*, 22, doi:10.1186/s12951-020-0580-1.
16. Lim, J.; Yeap, S.P.; Che, H.X.; Low, S.C. Characterization of Magnetic Nanoparticle by Dynamic Light Scattering. *Nanoscale Res Lett* **2013**, *8*, 381, doi:10.1186/1556-276X-8-381.
17. Sandler, S.E.; Fellows, B.; Mefford, O.T. Best Practices for Characterization of Magnetic Nanoparticles for Biomedical Applications. *Anal. Chem.* **2019**, *91*, 14159–14169, doi:10.1021/acs.analchem.9b03518.
18. Hurt, D.; Li, S.; Amann, A. Versatile SQUID Susceptometer With Multiple Measurement Modes. *IEEE Transactions on Magnetics* **2013**, *49*, 3541–3544, doi:10.1109/TMAG.2013.2241029.
19. Nieciecka, D.; Rękorajska, A.; Cichy, D.; Końska, P.; Żuk, M.; Krysiński, P. Synthesis and Characterization of Magnetic Drug Carriers Modified with Tb3+ Ions. *Nanomaterials* **2022**, *12*, 795, doi:10.3390/nano12050795.
20. Ludwig, F.; Guillaume, A.; Schilling, M.; Frickel, N.; Schmidt, A.M. Determination of Core and Hydrodynamic Size Distributions of CoFe2O4 Nanoparticle Suspensions Using Ac Susceptibility Measurements. *Journal of Applied Physics* **2010**, *108*, 033918, doi:10.1063/1.3463350.
21. Ludwig, F.; Balceris, C.; Jonasson, C.; Johansson, C. Analysis of AC Susceptibility Spectra for the Characterization of Magnetic Nanoparticles. *IEEE Transactions on Magnetics* **2017**, *53*, 1–4, doi:10.1109/TMAG.2017.2693420.
22. Chantrell, R.; Popplewell, J.; Charles, S. Measurements of Particle Size Distribution Parameters in Ferrofluids. *IEEE Transactions on Magnetics* **1978**, *14*, 975–977, doi:10.1109/TMAG.1978.1059918.
23. Patterson, A.L. The Scherrer Formula for X-Ray Particle Size Determination. *Phys. Rev.* **1939**, *56*, 978–982, doi:10.1103/PhysRev.56.978.
24. Pietschmann, J.; Dittmann, D.; Spiegel, H.; Krause, H.-J.; Schröper, F. A Novel Method for Antibiotic Detection in Milk Based on Competitive Magnetic Immunodetection. *Foods* **2020**, *9*, 1773, doi:10.3390/foods9121773.
25. Pietschmann, J.; Spiegel, H.; Krause, H.-J.; Schillberg, S.; Schröper, F. Sensitive Aflatoxin B1 Detection Using Nanoparticle-Based Competitive Magnetic Immunodetection. *Toxins* **2020**, *12*, 337, doi:10.3390/toxins12050337.
26. Achtsnicht, S.; Pourshahidi, A.M.; Offenhäusser, A.; Krause, H.-J. Multiplex Detection of Different Magnetic Beads Using Frequency Scanning in Magnetic Frequency Mixing Technique. *Sensors* **2019**, *19*, 2599, doi:10.3390/s19112599.
27. Pourshahidi, A.M.; Achtsnicht, S.; Nambipareechee, M.M.; Offenhäusser, A.; Krause, H.-J. Multiplex Detection of Magnetic Beads Using Offset Field Dependent Frequency Mixing Magnetic Detection. *Sensors* **2021**, *21*, 5859, doi:10.3390/s21175859.
28. Achtsnicht, S.; Neuendorf, C.; Faßbender, T.; Nölke, G.; Offenhäusser, A.; Krause, H.-J.; Schröper, F. Sensitive and Rapid Detection of Cholera Toxin Subunit B Using Magnetic Frequency Mixing Detection. *PLOS ONE* **2019**, *14*, e0219356, doi:10.1371/journal.pone.0219356.
29. Rabehi, A.; Garlan, B.; Achtsnicht, S.; Krause, H.-J.; Offenhäusser, A.; Ngo, K.; Neveu, S.; Graff-Dubois, S.; Kokabi, H. Magnetic Detection Structure for Lab-on-Chip Applications Based on the Frequency Mixing Technique. *Sensors* **2018**, *18*, 1747, doi:10.3390/s18061747.
30. Engelmann, U.M.; Shalaby, A.; Shasha, C.; Krishnan, K.M.; Krause, H.-J. Comparative Modeling of Frequency Mixing Measurements of Magnetic Nanoparticles Using Micromagnetic Simulations and Langevin Theory. *Nanomaterials* **2021**, *11*, 1257, doi:10.3390/nano11051257.
31. Krishnan, K.M. *Fundamentals and Applications of Magnetic Materials*; Oxford University Press, 2016; ISBN 978-0-19-957044-7.
32. Granqvist, C.G.; Buhrman, R.A. Ultrafine Metal Particles. *Journal of Applied Physics* **1976**, *47*, 2200–2219, doi:10.1063/1.322870.
33. Comparison of Volume Distribution of Magnetic Nanoparticles Obtained from M-H Curve with a Mixture of Log-Normal Distributions: Journal of Applied Physics: Vol 117, No 17 Available online: https://aip.scitation.org/doi/10.1063/1.4919268 (accessed on 27 June 2022).

34. Krause, H.-J.; Wolters, N.; Zhang, Y.; Offenhäusser, A.; Miethe, P.; Meyer, M.H.F.; Hartmann, M.; Keusgen, M. Magnetic Particle Detection by Frequency Mixing for Immunoassay Applications. *Journal of Magnetism and Magnetic Materials* **2007**, *311*, 436–444, doi:10.1016/j.jmmm.2006.10.1164.
35. Jefremovas, E.M.; Gandarias, L.; Rodrigo, I.; Marcano, L.; Grüttner, C.; García, J.Á.; Garayo, E.; Orue, I.; García-Prieto, A.; Muela, A.; et al. Nanoflowers Versus Magnetosomes: Comparison Between Two Promising Candidates for Magnetic Hyperthermia Therapy. *IEEE Access* **2021**, *9*, 99552–99561, doi:10.1109/ACCESS.2021.3096740.
36. Pongrac, I.M.; Dobrivojević, M.; Ahmed, L.B.; Babič, M.; Šlouf, M.; Horák, D.; Gajović, S. Improved Biocompatibility and Efficient Labeling of Neural Stem Cells with Poly(L-Lysine)-Coated Maghemite Nanoparticles. *Beilstein J. Nanotechnol.* **2016**, *7*, 926–936, doi:10.3762/bjnano.7.84.
37. Riahi, K.; Rietberg, M.T. Effect of Changing Iron Content and Excitation Frequency on Magnetic Particle Imaging Signal: A Comparative Study of Synomag® Nanoparticles. **2021**, *15*, 4.
38. Liu, S.; Chiu-Lam, A.; Rivera-Rodriguez, A.; DeGroff, R.; Savliwala, S.; Sarna, N.; Rinaldi-Ramos, C.M. Long Circulating Tracer Tailored for Magnetic Particle Imaging. *Nanotheranostics* **2021**, *5*, 348–361, doi:10.7150/ntno.58548.
39. Kallumadil, M.; Tada, M.; Nakagawa, T.; Abe, M.; Southern, P.; Pankhurst, Q.A. Suitability of Commercial Colloids for Magnetic Hyperthermia. *Journal of Magnetism and Magnetic Materials* **2009**, *321*, 1509–1513, doi:10.1016/j.jmmm.2009.02.075.
40. Shahbazi-Gahrouei, D.; Abdolahi, M. Superparamagnetic Iron Oxide-C595: Potential MR Imaging Contrast Agents for Ovarian Cancer Detection. *Journal of Medical Physics* **2013**, *38*, 198, doi:10.4103/0971-6203.121198.
41. Dennis, C.L.; Krycka, K.L.; Borchers, J.A.; Desautels, R.D.; van Lierop, J.; Huls, N.F.; Jackson, A.J.; Gruettner, C.; Ivkov, R. Internal Magnetic Structure of Nanoparticles Dominates Time-Dependent Relaxation Processes in a Magnetic Field. *Advanced Functional Materials* **2015**, *25*, 4300–4311, doi:10.1002/adfm.201500405.
42. Lévy, M.; Gazeau, F.; Bacri, J.-C.; Wilhelm, C.; Devaud, M. Modeling Magnetic Nanoparticle Dipole-Dipole Interactions inside Living Cells. *Phys. Rev. B* **2011**, *84*, 075480, doi:10.1103/PhysRevB.84.075480.
43. Branquinho, L.C.; Carrião, M.S.; Costa, A.S.; Zufelato, N.; Sousa, M.H.; Miotto, R.; Ivkov, R.; Bakuzis, A.F. Effect of Magnetic Dipolar Interactions on Nanoparticle Heating Efficiency: Implications for Cancer Hyperthermia. *Sci Rep* **2013**, *3*, 2887, doi:10.1038/srep02887.
44. Oyarzún, S.; Tamion, A.; Tournus, F.; Dupuis, V.; Hillenkamp, M. Size Effects in the Magnetic Anisotropy of Embedded Cobalt Nanoparticles: From Shape to Surface. *Sci Rep* **2015**, *5*, 14749, doi:10.1038/srep14749.
45. Shasha, C.; Teeman, E.; Krishnan, K.M. Nanoparticle Core Size Optimization for Magnetic Particle Imaging. *Biomed. Phys. Eng. Express* **2019**, *5*, 055010, doi:10.1088/2057-1976/ab3972.
46. Yu, E.Y.; Bishop, M.; Zheng, B.; Ferguson, R.M.; Khandhar, A.P.; Kemp, S.J.; Krishnan, K.M.; Goodwill, P.W.; Conolly, S.M. Magnetic Particle Imaging: A Novel in Vivo Imaging Platform for Cancer Detection. *Nano Lett.* **2017**, *17*, 1648–1654, doi:10.1021/acs.nanolett.6b04865.
47. Engelmann, U.M.; Shasha, C.; Teeman, E.; Slabu, I.; Krishnan, K.M. Predicting Size-Dependent Heating Efficiency of Magnetic Nanoparticles from Experiment and Stochastic Néel-Brown Langevin Simulation. *Journal of Magnetism and Magnetic Materials* **2019**, *471*, 450–456, doi:10.1016/j.jmmm.2018.09.041.
48. Lima, E.; De Biasi, E.; Mansilla, M.V.; Saleta, M.E.; Granada, M.; Troiani, H.E.; Effenberger, F.B.; Rossi, L.M.; Rechenberg, H.R.; Zysler, R.D. Heat Generation in Agglomerated Ferrite Nanoparticles in an Alternating Magnetic Field. *J. Phys. D: Appl. Phys.* **2013**, *46*, 045002, doi:10.1088/0022-3727/46/4/045002.